

pubs.acs.org/JPCA Article

Spectroscopic Signatures of Mode-Dependent Tunnel Splitting in the Iodide-Water Binary Complex

Published as part of The Journal of Physical Chemistry virtual special issue "International Symposium on Molecular Spectroscopy".

Justin J. Talbot,[#] Nan Yang,[#] Meng Huang,[#] Chinh H. Duong, Anne B. McCoy,* Ryan P. Steele,* and Mark A. Johnson*



Cite This: J. Phys. Chem. A 2020, 124, 2991-3001



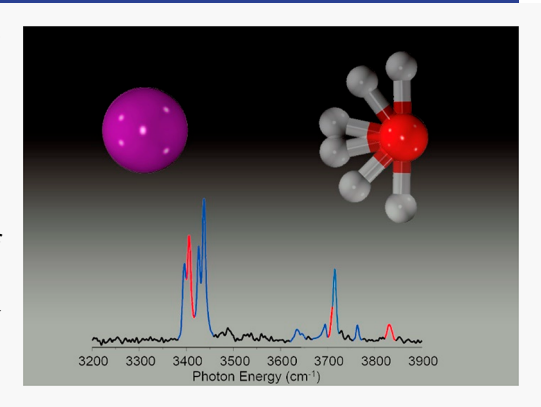
ACCESS

Metrics & More

Article Recommendations

si Supporting Information

ABSTRACT: The gas-phase vibrational spectrum of the isolated iodide—water cluster ion ($I^-\cdot H_2O$), first reported in 1996, presents one of the most difficult, long-standing spectroscopic puzzles involving ion microhydration. Although the spectra of the smaller halides are well described in the context of an asymmetrical ground-state structure in which only one OH group is hydrogen-bonded to the ion, the $I^-\cdot H_2O$ spectrum displays multiplet structures with partially resolved rotational patterns that are additionally influenced by quantum nuclear spin statistics. In this study, this complex behavior is unraveled with a combination of experimental methods, including ion preparation in a temperature-controlled ion trap and spectral simplification through applications of tag-free, two-color IR—IR double-resonance spectroscopy. Analysis of the double-resonance spectra reveals a vibrational ground-state tunneling splitting of about 20 cm $^{-1}$, which is on the same order as the spacing between the peaks that comprise the multiplet



structure. These findings are further supported by the results obtained from a fully coupled, six-dimensional calculation of the vibrational spectrum. The underlying level structure can then be understood as a consequence of experimentally measurable, vibrational mode-dependent tunneling splittings (which, in the case of the ground vibrational state, is comparable to the rotational energy spacing between levels with $K_a = 0$ and 1), as well as Fermi resonance interactions. The latter include the hydrogen-bonded OH stretches and combination bands that involve the HOH bend overtones and soft-mode excitations of frustrated translation and rotation displacements of the water molecule relative to the ion. These anharmonic couplings yield closely spaced bands that are activated in the IR by borrowing intensity from the OH stretch fundamentals.

INTRODUCTION

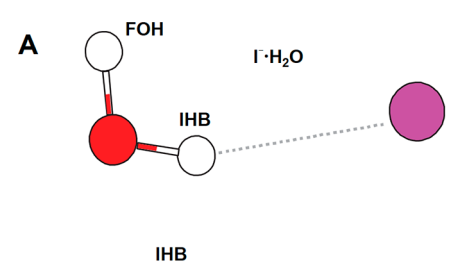
The vibrational spectrum of the iodide-water binary complex, I-H2O, was the first of this class of halide monohydrate ions to be reported in 1996 by Okumura and co-workers. This seminal study ushered in a new field that has shaped our understanding of ion hydration. 1,2 Subsequent studies of the $X^- \cdot H_2O$ (X = F, Cl, Br, I) systems and their isotopologues, over the expanded frequency range of 600-4000 cm⁻¹, have provided a detailed picture of their vibrational level structures, which, in turn, have yielded stringent constraints on the potential energy surfaces that drive halide ion hydration.^{3–13} In most cases, the X-·H2O spectral features have been convincingly assigned to the expected normal-mode fundamentals, overtones, and combination bands based on C_s equilibrium structures, such as the configuration depicted in Figure 1A. On the other hand, I-H₂O spectrum, recorded in the course of this work and displayed in Figure 1B, stands out as one of the most complex of the halide series with many labeled features in Figure 1B remaining unassigned after more than two decades of study.

A partial assignment emerges from temporarily overlooking the detailed multiplet structures and focusing instead on the two sets of transitions centered near 3400 and 3700 cm⁻¹. Specifically, the asymmetric equilibrium structure of the I⁻·H₂O complex (Figure 1A) qualitatively accounts for the widely split pattern in the OH stretching region in a scheme where the strong set of bands (β_{13-16} near 3400 cm⁻¹) have been nominally assigned to the red-shifted OH group that is bound to the ion (hereafter denoted IHB for "ionic hydrogenbonded").^{5,6} The weaker features centered at 3714 cm⁻¹

Received: January 30, 2020 Revised: March 5, 2020 Published: March 12, 2020







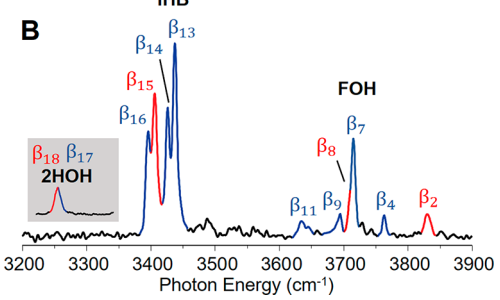


Figure 1. Asymmetric minimum-energy structure of $I^-\cdot H_2O$ and its vibrational predissociation spectrum. (A) Minimum-energy structure of $I^-\cdot H_2O$ from the MB-nrg potential. (B) Vibrational predissociation spectrum of $I^-\cdot H_2O$ at 20 K with low laser power to ensure that the maximum number of photons absorbed at any transition is one (linear regime). The inset highlighted by the gray background is an Ar-messenger tagged predissociation spectrum in the same region to reveal transitions to states that lie below the iodide-water dissociation threshold. See text for the meaning of the red and blue highlights.

(labeled β_{2-11}) are then expected for free OH group (denoted FOH). Some of the differences in the fine structure associated with these motions can then be attributed to the differences in the transition types: bands with the transition to the fundamental in the IHB being primarily parallel, and those involving the fundamental in the FOH displaying mixed parallel and perpendicular character. Spectroscopically, the two different transition types lead to primarily $\Delta K_a = 0$ rovibrational transitions carrying most of the intensity for the IHB motion, which would result in a single feature (at this rather modest resolution of ~ 3 cm⁻¹) in the lower-energy region. The component of the transition moment that is perpendicular to the IO axis for the FOH transition would lead to strong transitions with $\Delta K_a = \pm 1$, and, indeed, the extra peaks in the FOH region have been attributed to partially resolved rotational structure.⁶ This difference in transition types can be traced to the angles between the two OH bonds (which are roughly the orientations of the transition moments) and the IO axis (which is approximately the a rotational axis for this ion), as well as the expected partial locality of the OH stretching

While the above description qualitatively accounts for some of the observed fine structure, it does not explain the curious quartet structure (β_{13-16} in Figure 1B) of the IHB region near 3400 cm⁻¹, which was first reported by Okumura and coworkers. This feature is absent in other halide—water complexes, for example, as well as in the Ar-tagged spectrum of $I^-\cdot H_2O$. One aspect of the ion—water interaction that complicates the $I^-\cdot H_2O$ spectrum relative to the smaller halides is that its barrier to exchanging the bound OH group with the free OH group is smallest in the halide series. Earlier calculations 8,14 placed this barrier at 105-185 cm⁻¹, while more recent work supports the smaller value, reporting a barrier of 102 cm⁻¹. These values can be compared to the frequency (~ 160 cm⁻¹) attributed to the in-plane bending

mode, ⁸ which is the motion that connects the two equivalent minima on the potential surface through the $C_{2\nu}$ transition-state structure. The similarity of this frequency to the height of the barrier points to a scenario in which the ground vibrational state should exhibit relatively large tunneling splittings. These splittings would be expected to be partially quenched with OH stretch excitation, however, due to the larger effective barrier when an anharmonic $\nu=1$ state is accessed. This behavior could account for doublets in the OH-stretching regions, but it nevertheless does not explain the quartet structure observed in the IHB region of the spectrum nor the series of transitions in the FOH region.

In the present study, the I-H₂O spectrum is revisited using tools that have been developed over the past decade. On the experimental side, these developments include the ability to control clusters' internal energy using cryogenic ion traps and the ability to obtain linear spectra without the need for a weakly bound adduct (mass tag) using two-color IR-IR double-resonance spectroscopy. These approaches are combined with knowledge of the frequencies of the six vibrations in this ion from the argon-tagged I-H2O spectrum over a broader spectral range,8 along with theoretical predictions of the level structure by application of a fully coupled, six-dimensional eigensolver model on a new, MB-nrg many-body potential energy surface. 3,7,11 These methods yield a consistent assignment scheme and reveal how vibrational mode-dependent tunneling splittings, softmode combination bands, and partially resolved rotational fine structure (modified by nuclear spin statistics) all combine to yield the observed multiplet patterns in the spectrum of the cold I[−]·H₂O complex.

OVERVIEW OF EXPERIMENTAL AND COMPUTATIONAL APPROACHES

Experimentally, the I-H2O cluster was prepared with electrospray ionization and cooled in a temperature-controlled ion trap that has been described previously, 15,20 and its vibrational spectrum was recorded by infrared photodissociation with several complementary laser configurations. 15,20 The dissociation energy of this complex has been reported to be in the range of 3410-3510 cm⁻¹ using threshold electron photodetachment of the anion,²¹ which lies in middle of the OH stretching range. As such, a changeover from one- to twophoton dissociation will occur, depending on whether the upper state in the transition lies above or below the dissociation energy and, in the case of the former, the dissociation lifetime of the metastable state. This effect was explored by reducing the laser pulse energy to avoid multiphoton absorption so that transitions to states with energies below the dissociation threshold (after accounting for residual internal energy) are suppressed in the spectrum. For example, the bend overtone mode near 3200 cm⁻¹ is missing in the low-power, linear predissociation (PD) spectrum (complete trace in Figure 1B) but can be observed using Ar-tagging methods (gray inset in Figure 1B); this observation establishes that the effective dissociation energy at the experimental temperature lies between 3200 and 3400 cm⁻¹. As discussed below, the discrepancy between these values and the previously reported dissociation energy²¹ is likely due to the fact that the excited states accessed in the transitions shown in Figure 1 near 3400 cm $^{-1}$ (β_{13-16}) are situated just above dissociation threshold but are surprisingly long-lived. ²² Steps taken to confirm that the spectrum shown in Figure 1 results from the

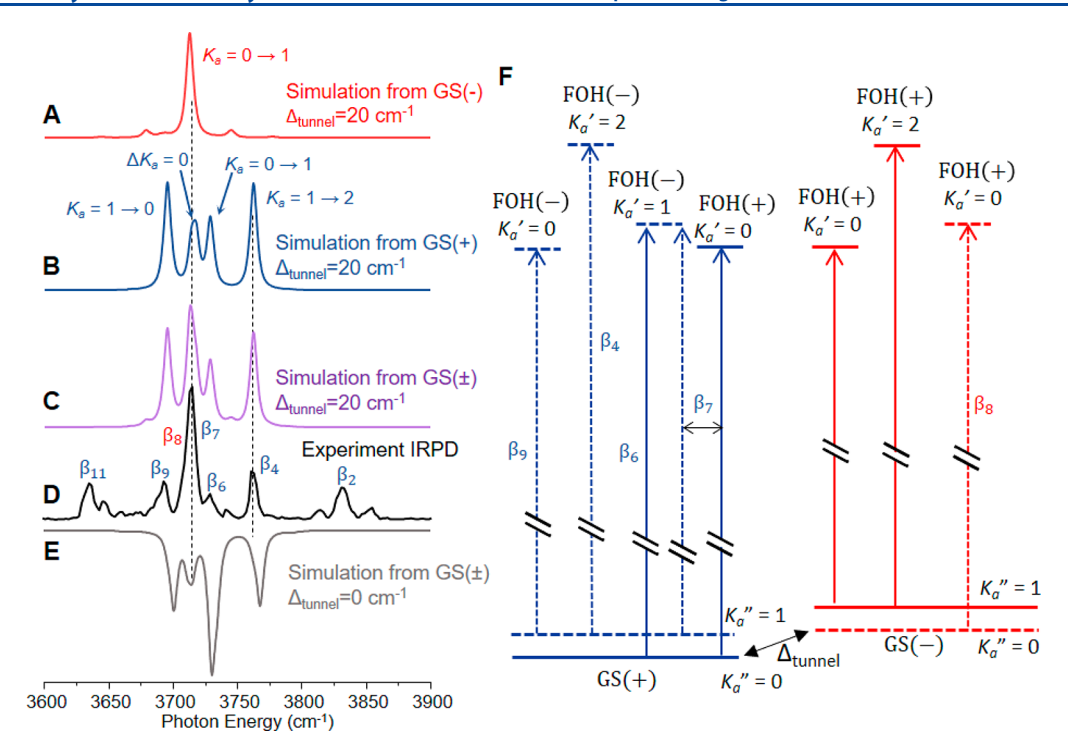


Figure 2. Comparison between simulated FOH spectra based on different tunneling splittings with the experimental spectrum at 20 K. (A, B) Simulated rovibrational spectrum based on a 20 cm⁻¹ ground-state tunneling splitting for transitions originating from K_a levels built off of the GS(-) and GS(+) states, respectively. (C) Simulated spectrum with a 20 cm⁻¹ ground-state tunneling splitting initiated from all thermally populated $GS(\pm)$ and K_a levels, including nuclear spin statistical effects. (D) Experimental IR predissociation spectrum. (E) Simulated spectrum obtained with a 0 cm⁻¹ tunneling splitting, based on thermally populated $GS(\pm)$ and K_a levels. (F) Energy level diagram illustrating the transitions involved, in which the solid and dashed lines are used to differentiate between states that are symmetric (solid) and antisymmetric with respect to exchange of the two hydrogen atoms. The tunneling splitting between GS(-) and GS(+) is indicated with the double-sided arrow (Δ_{tunnel}).

absorption of a single photon are discussed in the Supporting Information (S2). Two-photon processes could be observed by increasing the laser fluence above that used to obtain the spectrum in Figure 1 by about a factor of 3.

When a PD spectrum is heterogeneous (because of isomers, rotational and/or vibrational state populations, and, in this case, tunneling splittings), overlapping spectral contributions from different ground-state populations can be isolated with two-color, IR-IR double-resonance hole-burning spectroscopy. 15 These spectra were measured using the IR 2MS capability of the photofragmentation mass spectrometer, 15 where massselected ions were irradiated with the pump laser first and mass-separated in the secondary mass spectrometer to eliminate the photofragment from the pump. The remaining parent ion was then irradiated by the probe laser and massseparated again in the third mass-separation stage, where the fragment from the probe laser was monitored. When acquiring a ground state-selective, double-resonance dip spectrum, the probe laser was fixed on a frequency that is potentially unique to one of the components that contribute to the overall spectrum. The pump laser was then scanned through the entire spectrum, and when it excited transitions originating from the level monitored by the probe laser, the probe-laser fragment yield was decreased. These depletions were recorded as a function of pump-laser frequency, and the resulting "dip" trace reveals the spectrum associated with the rovibrational state selected by the probe laser. More complicated patterns, including those featuring photoinduced enhancement of the fragment from the probe laser, were also observed when the states excited by the pump laser were either stable or exhibited longer dissociation lifetimes than the time between the pump

and probe excitations (about 30 μ s). This scenario is relevant to the present IR–IR studies because, as mentioned above, many of the upper levels in the OH stretching region of the I $^-$ ·H $_2$ O spectrum are sufficiently long-lived to display such enhancement. Although excited-state dynamics are complex and likely state-dependent, this situation was exploited to gain qualitative insight into the quantum composition of the levels involved in the quartet, as discussed in the Supporting Information (Figures S3.4 and S3.5).

Calculations of the rovibrational spectra were performed via numerical solution of the Schrödinger equation in a basis set of six-dimensional harmonic oscillators and prolate symmetric top basis functions. In this calculation, five of the six available internal degrees of freedom were represented as normal-mode coordinates that were computed at the C_{2y} reference structure. The sixth degree of freedom, the in-plane bend, was described by a rigid, curvilinear rotation of the water molecule about the principal axis that is perpendicular to the plane of the molecule and intersects the molecule at its center of mass. Eight quanta of excitation were included in all normal-mode coordinates except the in-plane bend, which, as a result of the double-well anharmonicity, required ten quanta for convergence. Gauss-Hermite quadrature was used for evaluating the potentialenergy and dipole-moment integrals. The large size of the resulting vibrational Hamiltonian matrix required the use of the PRIMME iterative diagonalization routine. 18 After exhaustive benchmarking, the six-dimensional potential energy calculations of I-H2O were performed with the analytic MBnrg potential energy surface. 23 The dipole moment hypersurfaces were calculated using the MP2 level of theory with the aug-cc-pVTZ-PP basis set within the frozen-core approximation. 24 All dipole moment calculations were performed using a development version of the Q-Chem software package. 17 The rotation constants were computed for each vibrational state by averaging over the fully coupled, six-dimensional vibrational wave functions. The axes were defined, starting from the C_{2v} reference structure, by aligning the a axis with the C_2 symmetry axis and the c axis perpendicular to the plane of the molecule. Full details of these calculations, including extension to a vibrationally adiabatic approach, are provided in the Supporting Information.

ASSIGNMENTS OF PARTIALLY ROTATIONALLY RESOLVED VIBRATIONAL BANDS

The spectroscopic assignments in the following discussion are made in two parts. In the first, an analysis of the rotational structure of the bands near $3700~\rm cm^{-1}$ is performed in order to obtain an approximate ground-state tunneling splitting. This discussion is then followed by an analysis of the quartet feature near $3400~\rm cm^{-1}$.

Figure 2D presents an expanded version of the experimental spectrum in the region of the FOH fundamental. Above the spectrum (purple trace, C, of Figure 2) are the results of a spectral simulation, performed using PGOPHER²⁶ with parameters that are provided in Table S1.3 of the Supporting Information. These parameters include the transition dipole moments and vibrationally averaged rotational constants, which were obtained from the six-dimensional calculation, described above, as well as the tunneling splitting and FOH transition frequency, which were adjusted to obtain agreement with the measured spectrum. This purple trace is the sum of traces A (red) and B (blue) in Figure 2. Those traces isolate the contributions from transitions originating from the lower [GS(+), blue] and upper [GS(-), red] members of the tunneling doublet. Figure 2F depicts the rovibrational level structure corresponding to these transitions. In this panel, solid and dashed lines are used to differentiate states that are symmetric (solid) and antisymmetric (dashed) with respect to exchange of the two hydrogen atoms. When the ground-state tunneling splitting is small, the lowest-energy state that is antisymmetric with respect to exchange of the hydrogen atoms is the $K''_a = 0$ level of the GS(-) member of the tunneling doublet, and this level will have three times the population of the $K_a'' = 0$ level in the GS(+) manifold, due to nuclear spin statistics. On the other hand, when the tunneling splitting is larger than the energy of the $K''_a = 1$ level of the GS(+)member, the $K_a'' = 1$ level of the GS(+) tunneling member will become the lowest-energy antisymmetric state and have three times the population of the $K_a'' = 0$ level of the GS(+)manifold. The latter situation is illustrated in panel F. The population of higher-energy states within either symmetry class (with respect to exchange of the hydrogen atoms) will be determined by the usual temperature-dependent Boltzmann

Since the tunneling splitting is expected to be mostly quenched by excitation of one of the OH stretches, the red pattern of transitions in Figure 2 will shift relative to the blue pattern by roughly the value of the ground-state tunneling splitting. This shift is the origin of the difference between traces C and E of Figure 2, while the 3:1 nuclear spin weighting for population of the K_a'' levels is the reason for the different intensity patterns of the blue and red traces in Figure 2. The important point is that, when the GS(\pm) tunneling splitting is taken to be small (trace E of Figure 2), the

simulated trace does not match the recorded trace (D in Figure 2). The agreement improves dramatically when a ground-state tunneling splitting of 20 cm⁻¹ and an excited state tunneling splitting of -2 cm⁻¹ are used. The 20 cm⁻¹ value for the ground-state tunneling splitting is accidentally close to the ~ 17 cm⁻¹ energy difference between $K_a'' = 1$ and $K_a'' = 0$ levels in this ion. Therefore, the main component of the FOH rovibrational profile can be captured by a combination of vibrational tunneling in the soft in-plane bend mode, rotational fine structure, and nuclear spin-weighted state populations.

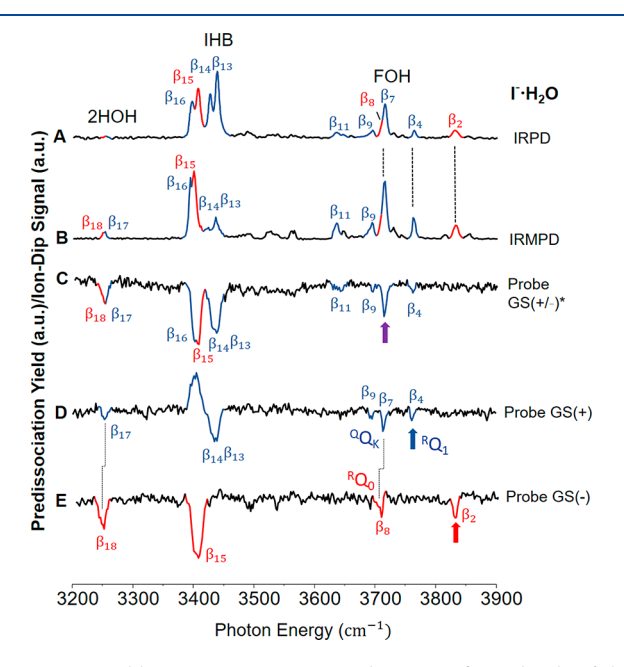


Figure 3. Double-resonance spectra, probing specific K_a levels of the ground vibrational state(s). (A) Linear infrared photodissociation spectrum obtained with low laser power (0.7 mJ/pulse, 8 ns pulse width, 5 mm beam diameter) at 20 K. (B) High-power (20 mJ/pulse) IRMPD experimental spectrum at 20 K. (C) Experimental state-specific double-resonance spectra obtained by probing the peak indicated by the purple arrow, which putatively includes population from both GS(+) and GS(-) states. The main contribution is nonetheless attributed to GS(+), arising from the β_8 transition, and the remaining contribution of GS(-) arises from the β_8 transition. (D, E) Double-resonance spectra obtained by probing the peaks indicated by the color-coded arrows, which reflect the GS(+) and GS(-) populations, correspondingly.

To further explore the magnitude of the tunneling splitting and the assignment of the spectrum in the region of the quartet, the results of two-color, IR-IR double-resonance experiments have been analyzed. In this part of the study, the probe laser was fixed at three features in the rotational contour of the FOH feature. The resulting spectra are shown in panels C to E of Figure 3, where the probe frequency is indicated by the colored arrow. These spectra were obtained at higher laser power (Figure 3B) than the trace reported in Figure 1B, which has been reproduced (Figure 3A) for comparison. The patterns in the two power regimes differ in the region of the lowerenergy bands in the bend overtone and IHB regions (β_{13-18}), while the FOH structure generally remains intact. As mentioned above, the appearance of $\beta_{17.18}$ at higher power in a single-laser experiment is due to the fact that the excited state (the v = 2 level of the bending mode, denoted 2HOH) lies below the dissociation threshold of the ion. The powerdependent intensity profiles of the β_{13-16} features that make up the quartet are more complicated. These effects arise because the involved excited states are long-lived and exhibit highly structured, mode-dependent absorption spectra that mediate the cross section for absorption of a second photon at the excitation frequency, which is needed to accelerate dissociation sufficiently to yield a strong fragment signal (Figure S3.4).

Importantly, two distinct spectral patterns of transitions are revealed in the IR-IR double resonance scans between 3600 and 3900 cm⁻¹, which are consistent with spectra that originate from contributions of two different symmetry classes in the ground-state population. This effect is immediately evidenced by the character of the dips in parts D and E of Figure 3 that arise from the two peaks comprising the doublet feature near 3400 cm⁻¹ in traces A and B of Figure 3. (The closely spaced doublet characters of this feature— $\beta_{13,14}$ and $\beta_{15,16}$ in trace A of Figure 3—are lost due to the saturation conditions required to observe the dip pattern.) In trace E, only the lower-energy member of the main IHB doublet is depleted when the probe is set at β_2 (3831 cm⁻¹), while in trace C of Figure 3, with a probe set at a possible overlap of β_7 and β_8 (3714 cm⁻¹), both members of the 3400 cm⁻¹ doublet are depleted similarly. Probing at 3763 cm⁻¹ (β_4 , trace D of Figure 3) yields a more complicated pattern in which the lower member of the main doublet is enhanced, indicating that excitation by the pump creates an excited state that exhibits absorption at the probe frequency (see Figure S3.4C, where excitation of β_{16} creates new absorption around the β_4 band). These features of the IR-IR study that reveal state-selective spectra and excited-state dynamics warrant further study and analysis, but the present investigation is mostly concerned with the implications of these more advanced measurements on assignment of the linear spectrum of the cold, ground-state complex.

Turning to the quartet and bend-overtone regions at the lower-energy part of the spectral range covered in Figure 3, the results of the double-resonance experiment were found to be consistent with the conclusions described above regarding the symmetry assignments of the rotational bands. Specifically, trace E exclusively records lower-frequency features of the tunneling doublet transitions (originating in GS(-), which is higher in energy), and only the lower-energy IHB peak yields a dip in the probe signal. As this trace also includes the β_8 peak that was assigned in the rotational analysis (Figure 2C) to correspond to the $K_a = 1 \leftarrow 0$ transition from GS(-), this trace is associated with transitions originating from the GS(-)level with $K_a'' = 0$. On the other hand, traces C and D of Figure 3 include contributions from the GS(+) level, and the fact that trace D shows a dip feature at the location of the higher-energy member of the doublet $(\beta_{13,14})$ in the IHB region indicates that it originates the from GS(+) manifold. Due to the positive signal in the energy range of the lower member ($\beta_{15,16}$), an assignment of this feature to one or both members of the ground-state tunneling doublet cannot be made based on this double-resonance response alone. Additional evidence that the transitions probed in panel D arise from GS(+), while those in panel E arise exclusively from GS(-), however, comes from the small (4 cm⁻¹) but significant shift of the position of the feature that is assigned to the overtone in the HOH bend (β_{17} and β_{18}). If the tunneling splitting for this excited bending state is identical to that for the ground state, these two transitions would appear at the same energy in these two IR²MS³ traces. This small observed shift is, therefore, consistent with a slightly smaller tunneling splitting (by $\sim 4 \text{ cm}^{-1}$) for the $\nu = 2$ level of the HOH bend, compared to the ground-state tunneling splitting. Accordingly, traces D and E of Figure 3 likely originate solely from different members of the GS tunneling pair.

Trace 3C is more complex in that it shows a broadened feature near 3250 cm⁻¹, compared to traces D and E of Figure 3, indicating that both GS(+) and GS(-) levels contribute to the probed transition at 3714 cm⁻¹. The relative contributions are complicated, however, by the admixture in the absorption at the probe wavelength (3714 cm⁻¹) and the efficiencies with which transitions excited by the pump laser remove population from the two lower levels under partially saturated excitation conditions (Figure S3.3). For example, the behavior of the rotational bands in the FOH region is most similar to the behavior displayed by the GS(+) ground state, indicating that the contribution from GS(-) to the probe fragmentation yield is less than that of GS(+). This conclusion is consistent with the analysis of the FOH band contour in Figure 2, where transitions from both GS(-) and GS(+) were found to contribute to the transition selected by the probe and identified as $\beta_{7.8}$. The smaller contribution from transitions arising from GS(-) is also consistent with the absence of the β_2 feature from trace C of Figure 3 and the redshift of the β_8 feature in trace E of Figure 3, relative to the position of the β_7 feature in trace D of Figure 3.

With this experimental confirmation of the assignments in place, an estimate of the tunneling splitting for both the ground and excited states can be made. In the rotational band assignments, the two features near the FOH band origin in trace D of Figure 3 were assigned to the $K_a = 0 \leftarrow 0 \ (\beta_7)$ and $K_a = 1 \leftarrow 0 \ (\beta_4)$ transitions that originate from the GS(+) level. As such, the shift between these two peaks is roughly the A rotational constant for the state with one quantum of excitation in the FOH vibration. In the absence of tunneling splitting in both vibrational states, the $K_a = 0 \leftarrow 0$ transition originating from GS(+) and the $K_a = 1 \leftarrow 0$ transition originating from GS(-) (β_8) should also be shifted by the value of the A rotational constant, which is approximately 17 cm⁻¹ (Table S3.1 and discussion thereafter). As noted above, these two transitions contributed to the broadening evident in the peak ($\beta_{7.8}$) near 3715 cm⁻¹ in trace C of Figure 3. The small displacement between the two dip peaks observed in the IR²MS³ spectra in this region (broken line in traces 3D and 3E) indicates that the difference between the tunneling splitting in the ground state and the tunneling splitting in the state with one quantum in the FOH is only slightly larger than 17 cm⁻¹. Analysis of the peak positions in the FOH region of the spectrum (Supporting Information, section S3) results in a ground-state tunneling splitting of approximately 20 cm⁻¹ and a splitting for the level with one quantum in the FOH of -2cm⁻¹, which are the parameters that were used to obtain traces B-D in Figure 2. Assuming similar tunneling behavior for the ν = 1 levels of the IHB and FOH modes, these splittings at least qualitatively account for the ~30 cm⁻¹ separation between the features assigned to the IHB near $3400~\mathrm{cm}^{-1}$ in traces A and B of Figure 3.

To this point, two of the four features in the IHB quartet can be understood as a consequence of a tunneling splitting in the ground vibrational state, which is manifest as a widely split doublet when recorded at high laser power (Figure 3C). These peaks are attributed to the two transitions involving excitation to the IHB(\pm) fundamental levels from the corresponding GS(\pm) states. The quartet then emerges in the lower-power

spectrum (Figure 1B) as the two more widely spaced band centers ($\beta_{13,14}$ and $\beta_{15,16}$) split into two closely spaced doublets (by $\sim 10 \text{ cm}^{-1}$). The roles of both electrical and mechanical anharmonicities in the generation of pervasive "extra" peaks in the spectra of the X-H₂O systems has been discussed at length, 8,10 and these resonance effects serve as a backdrop for the present analysis of the smaller splittings in the quartet feature. In a previous study of the spectrum of Ar-tagged I-H₂O₁⁸ for example, the vibrational frequencies of the six vibrational degrees of freedom in I-H2O were identified as band fundamentals or combination bands excited along with either the OH stretches or the overtone of the HOH bend. On the basis of the reported spectra, the soft modes associated with the IO stretch, in-plane water bend, and out-of-plane water bend modes were assigned at 131, 160, and 549 cm⁻¹, respectively. Using these values, both members of the tunneling doublet in states with two quanta in the HOH bend and one quantum in the IO stretch should lie close in energy to the corresponding IHB(-) fundamental. Similarly, the IHB(+) level lies close in energy to the state with two quanta in the HOH bend and one quantum of excitation in the in-plane bend $(2\nu_{\rm HOH} + \nu_{\rm IP})_{+}$. The frequencies of the transitions to these four states, based on the frequencies derived from ref 8, are plotted to-scale in the gray box in Figure 4. Combination-band activity has also been observed in both of these modes in many of the X-H₂O systems. As such, we propose that the two transitions expected from tunneling splitting in the IHB fundamental are further split by coupling to nearby, nominally dark levels composed of two quanta in the HOH bend plus one quantum of either the in-plane bend

One way to address the composition of vibrationally excited states that involve coupling between two or more contributions from the separable normal-mode basis is to monitor the

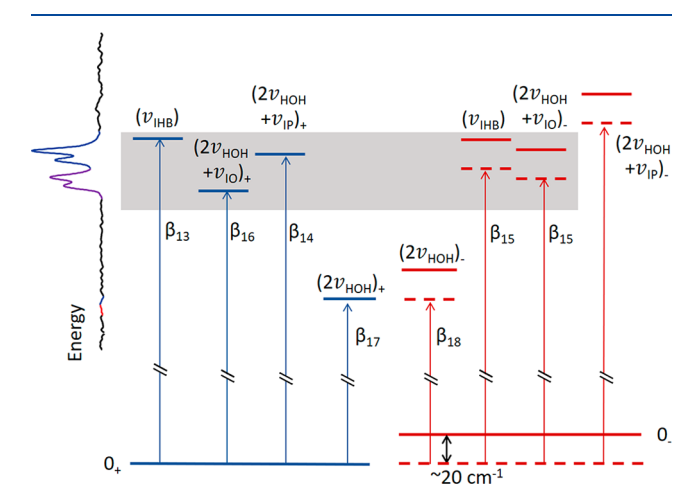


Figure 4. Energy-level diagram for the IHB region, based on previous spectral observations. The left inset is an IRPD spectrum reproduced from Figure 1B. The blue color of the energy level lines denotes the quantum states with (+) symmetry; the red color denotes (-) symmetry. The solid lines represent real energy levels, whereas dotted lines are shifted such that the initial state in the IR transitions is aligned with the (+) ground state for ease of comparison of transition energies (arrows). The shift (20 cm⁻¹) is the ground-state tunneling splitting, and the energies used to make the energy-level diagram are based on ref 8. The gray box shows the range of energies that correspond to the quartet feature in the spectrum (reproduced in inset).

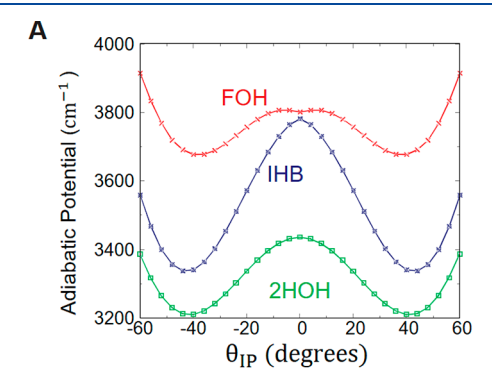
absorption spectra arising from the upper energy level in question. If the harmonic basis correctly describes this level, for example, the absorption spectrum will simply yield a spectrum that is identical to that of the ground state, but with slightly shifted transition energies that reflect the anharmonic coupling between modes. When the upper level is a superposition of zero-order states, however, its absorption spectrum should contain contributions from the two spectra arising from the two zeroth-order states that are coupled. The relevance of this attribute in the present case is that, if the close doublet features $(\beta_{13,14} \text{ and } \beta_{15,16})$ arise from coupling of the IHB fundamentals to states based on the bend overtone along with v = 1 levels of one or more soft modes, then the absorption spectrum should reflect the selection rules governing excitations from the v = 1level of the IHB as well as those from the v = 2 of the bend along with soft mode activity, as required to bring the v = 2 of the bend into resonance with v = 1 of the IHB stretch. The level diagram describing the spectra expected for the limiting (harmonic approximation) case as well as for that arising from mixed levels is presented in Figure S3.5.

A survey of the photofragmentation spectra, arising from excitation of each member of the quartet, is presented in Figure S3.4. In this experiment, the first laser was fixed at the frequency of one of the quartet bands, while the second laser was scanned from 600 to 4000 cm⁻¹. At first glance, one might expect that such a measurement would not yield any signal since the approach taken to obtain the spectra in Figure 1 and in trace A of Figure 3 relies on the states that are probed by the first laser dissociate. The fact that ground state depletions (Figure 3C-E) were observed, even though a significant fraction of the excited-state population survives the 30 μ s time between the pump and probe lasers, is consistent with a scenario where the lifetimes of these excited states are surprisingly long ($\geq 30 \mu s$). With these lifetime considerations in mind, the excited-state spectra of the upper levels of the four transitions (Figure S3.4) that make up the quartet are different in the region of the fundamental of the bend ($\sim 1600 \text{ cm}^{-1}$). In particular, traces D and F in Figure S3.4 exhibit one dominant feature, while traces C and E show a series of transitions separated by about 200 cm⁻¹. This behavior is consistent with the bands labeled β_{13} and β_{15} being assigned to the tunnel-split fundamental in the IHB, while the bands labeled β_{14} and β_{16} are better described as combination bands built off of the overtone in the HOH bend. When the spectra above 3400 cm⁻¹ are compared, traces C, E, and F appear more similar to each other than they do to trace D (red trace in Figure S3.4). This trend suggests that the transition that is probed by the fixed excitation laser in trace D originates from GS(-), whereas the transitions that are initially probed in the other three traces all originate from GS(+). A detailed analysis of the complex set of sharp bands displayed across the spectral range is beyond the scope of this paper, but the qualitative character of the state-specific spectra further supports the assignments of these four bands discussed above.

COMPARISON TO THE SPECTRUM PREDICTED BY FULL-DIMENSIONAL ANHARMONIC CALCULATIONS

The above discussion has been primarily based on the empirical analysis of the $I^-\cdot H_2O$ spectrum by fitting the rotational pattern and verifying the symmetries involved in the assignment scheme using IR–IR double resonance. But this approach did not consider the strength of the couplings

between the various zeroth-order excited states that govern the level pattern. Furthermore, the density of states stemming from combination bands and overtones of soft modes provides many additional possibilities for explaining the appearance of "extra" bands in the spectrum. The results of the full-dimensional vibrational eigensolver calculations—and adiabatic approximations thereof—are considered here, in order to further explore these interactions and their influence on the motions most responsible for the variety of observed bands.



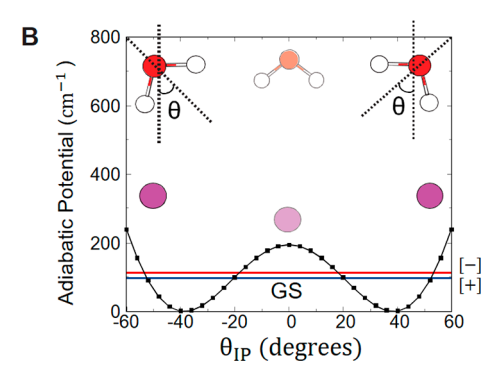


Figure 5. Mode-dependent tunnel splittings and adiabatic potential energy surfaces. (inset) Definition of the IP bend coordinate, along with (B) ZPE, (A) 2HOH, IHB, and FOH frequency-response curves added to the underlying double-well potential energy surface along the IP bend coordinate.

An adiabatic treatment of the I-H2O vibrations provides a conceptual (and semiquantitative) framework for understanding the mode-dependent tunneling behavior. This approach examines the manner in which the soft-mode potentials depend on the degree of excitation in the highfrequency motions. In this approximate treatment, the fivedimensional Schrödinger equation was solved as a function of the in-plane bend angle, θ_{ip} , which was defined as the angle between the vector that connects the oxygen and iodine atoms and the bisector of the HOH angle. These vectors intersect at the center of mass of HOH, as illustrated in the inset to panel B of Figure 5. The potential for the in-plane bend coordinate was calculated in the approximation that its potential energy is parametrically dependent on the eigenvalues of the other normal modes. The energy differences between the vibrationally adiabatic potential curves were then constructed as a function of $heta_{
m ip}$ by including the $heta_{
m ip}$ -dependence of the energies of states with varying degrees of excitation in the highfrequency modes.²⁷ In this manner, the four potential curves shown in Figure 5 can be considered as analogous to the

Born—Oppenheimer potentials in electronic structure calculations that differ according to the bonding character of the various electronic states. The one-dimensional Schrödinger equation, with an appropriate effective mass for the hindered in-plane rotation as defined in eq \$1.9,²⁸ can then be solved for each of these potentials, yielding tunneling splittings in the context of the vibrational eigenvalues on each of these surfaces. The spectrum in the OH stretching region can then be reconstructed from the energy gaps and transition dipole moments computed for transitions between the vibrational levels supported by the adiabatic surfaces. Additional information about the calculations of these potential curves can be found in section \$1.6 of the Supporting Information.

The GS potential within this adiabatic approximation is shown in panel B of Figure 5. The zero of energy for this and all of the adiabatic surfaces is taken to be the minimum of the ground-state adiabatic potential. The barrier on this surface is calculated to be ~200 cm⁻¹, giving rise to a 14.4 cm⁻¹ tunneling splitting between the first two vibrational levels supported by this double-minimum potential. This value is about 5 cm⁻¹ smaller than the splitting used to obtain the simulated spectrum shown in Figure 2 but is also within 1 cm⁻¹ of the value obtained from the full-dimensional eigensolver, discussed below. To put these results in context of previous reports, Horvath et al.8 placed the bare barrier to be about 300 cm⁻¹ with a corresponding tunneling splitting of ~4 cm⁻¹. The study of Paesani, Carrington, and co-workers, on the other hand, reported a splitting of 27.05 cm⁻¹ based on a fully coupled six-dimensional vibrational eigensolver calculation using the same MB-nrg potential, which exhibits a barrier along θ_{ip} of 101.63 cm⁻¹.

Excitation of the intramolecular HOH bend overtone does not appreciably change the shape of the one-dimensional adiabatic potential, as is seen by comparing the curve labeled 2HOH in Figure 5A (green) to the ground-state adiabatic potential in 5B (black). Conversely, the effective adiabatic barrier is significantly larger when the IHB stretching mode (blue) is excited, which is consistent with the empirically assigned quenching of the tunneling. Additionally, while the wave function associated with the bend overtone varies smoothly as a function of θ_{ip} , the wave functions associated with states with one quantum of excitation in one of the OH oscillators show a rapid change (and avoided crossing) near θ_{ip} = 0. While the nature of the vibrational states is subtler than implied by the above discussion when nonadiabatic contributions are considered,²⁷ the pattern of tunneling splittings for all but the FOH state is nonetheless consistent with the conclusions of the empirical analysis described above.

The fact that the $I^- H_2 O$ complex contains only four atoms, and it is one for which a high-accuracy potential energy surface is available, a raises the important question of whether computational tools are now refined to the point that observed anharmonic band patterns can be assigned from first principles. Such an advance would have a profound impact by expanding the complexity of systems amenable to experimental study without requiring the often-tedious methods of molecular spectroscopy, developed over decades, involving assignments with empirical parameters and effective Hamiltonians. To this end, the results of the fully coupled, six-dimensional calculations of the $I^- \cdot H_2 O$ spectrum are examined here. Comparisons of the resulting spectra to those shown in Figure 3 are provided in Figure 6, and the corresponding transition energies are collected in Table 1. A complete list of the

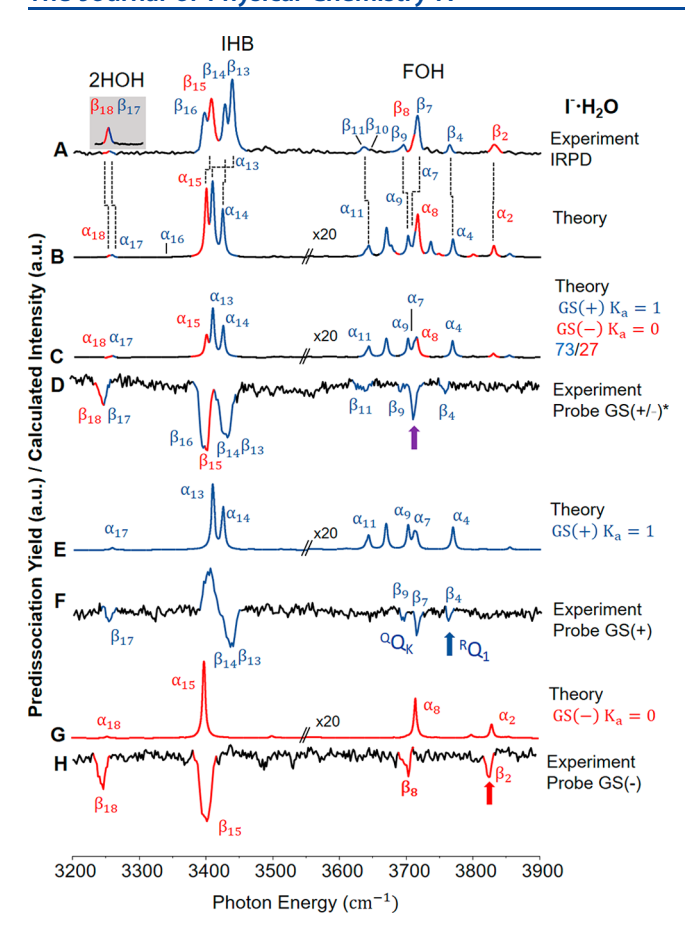


Figure 6. Comparison between the state-specific experimental and calculated spectra. (A) Linear infrared photodissociation spectrum obtained with low laser power (1 mJ/pulse, 8 ns pulse width, 5 mm beam diameter) at 20 K. (B) Calculated rovibrational spectrum at 20K. (C) Calculated spectrum initiated from both members of the ground-state tunneling pair, with the intensity scaled by 73% for GS(+) $K_a = 1$ and 27% for GS(-) $K_a = 0$. (D) Experimental state-specific, double-resonance spectra obtained by probing the peak indicated by the purple arrow, which includes population from both GS(+) and GS(-). (E, G) Calculated spectrum with the initial state being GS(+) and GS(-), respectively. (F, H) Double-resonance spectra obtained by probing the peaks indicated by the color-coded arrows, which reflect the GS(+) and GS(-) populations, correspondingly. The calculated intensities (traces B, C, E, G) in the FOH region are multiplied by 20.

energies of relevant states, along with assignments and vibrationally averaged rotational constants, is also provided in Table S1.3.

In general, this calculated spectrum (trace B, Figure 6) recovers the overall character of the observed bands (trace 6A), including much of the rotational fine structure associated with the FOH bands and the multiplet nature of the IHB. The predicted, vibrationally averaged A rotational constants for the ground and excited vibrational states involved in the transitions considered above are both 17 cm⁻¹, which are in agreement with the value that was used in the empirical analysis of the spectrum (see Table S3.1 and discussion thereafter). Additionally, the calculated ground-state tunneling splitting of 15 cm⁻¹ is similar to the splitting estimated with the vibrationally adiabatic approach (14.4 cm⁻¹), which highlights the accuracy of the latter method within the chosen potential energy surface. The origin of the discrepancy between the

present full-dimensional simulation (15 cm $^{-1}$ splitting) and the previous simulation by Paesani (27 cm $^{-1}$ splitting) is presently unclear. Possible candidates include the choice of vibrational coordinates and quadrature grids, as well as the neglect of subtle rotational couplings in the present calculations. The calculated tunneling splitting for the state with two quanta in the HOH bend is $10~{\rm cm}^{-1}$, which yields a separation between the GS(+) and GS(-) contributions to the HOH bend overtone feature of 4.4 cm $^{-1}$, close to the experimentally observed value of 4 cm $^{-1}$ (Figure 3). The tunneling splittings for the states with one quantum in the IHB and FOH are 6 and 4 cm $^{-1}$, respectively, and are significantly smaller than the ground-state tunneling splitting, as was also inferred from the simulated spectrum.

The calculated spectrum also explains the origin of the β_2 feature in the measured spectrum, which was left unassigned in the analysis of the rotational contour of the FOH fundamental. The calculations predict that this band arises from a transition between the upper member of the tunneling doublet [GS(-)] and the state with one quantum in the FOH mode and one quantum in the in-plane bend, denoted as FOH+IP(-). This assignment thus accounts for the fact that setting the probe laser at this transition effectively isolated the bands arising from the GS(-) level in Figure 3E.

The more complete six-dimensional (plus rotation) calculations also allow for the reconstruction of the spectrum from the contributions of specific symmetry and K rotational levels in the ground state. The simulated dip spectra from specific lower-state levels are displayed in panels C, E, and G of Figure 6. For example, the results shown in trace G in Figure 6 support the assignment scheme in which the aforementioned β_2 transition originates from GS(-) $K_a = 0$, and trace E in Figure 6 is consistent with the conclusion that the β_4 probe corresponds specifically to a transition originating from the $K_a = 1$ state of GS(+). The calculated spectra for both of these state-specific cases are generally in excellent agreement with the experimental dip spectra, including the subtle shifts observed in the $\beta_{17.18}$ and $\beta_{7.8}$ pairs. The calculated spectra do not reproduce the intensity pattern in the IHB quartet or bend overtone regions of the double-resonance experiments. This result is likely a consequence the high laser power (and likely multiphoton behavior) used for these experiments, however, and the calculated linear spectrum should not be expected to capture these effects. Both the calculations and the above rotational analysis predict that the relatively bright $\beta_{7.8}$ feature arises from overlapping transitions and accidental coincidence of the tunneling splitting and the A rotation constant. The double-resonance experiment, with the probe laser frequency set within this peak, provides an opportunity to test these predictions. In calculated trace C in Figure 6, transitions originating from GS(+) with $K_a = 1$ and GS(-)with $K_a = 0$ are included with their intensities provided in a 73:27 ratio, based on the experimental analysis of the bend overtone contributions. The calculated spectrum is in reasonable agreement, although the intensities in the FOH region from the GS(+) contribution are predicted to be larger. This behavior is also curiously inconsistent with a more detailed decomposition of the $\alpha_{7.8}$ band, shown in Figure S3.1. At the position of the probe laser, excitations of α_8 , rather than α_7 , would be predicted to dominate in trace C and D, based on the calculated spectra. Very subtle shifts of only a few wavenumbers in transitions α_7 , α_{83} , and α_{8} could be enough to shift these predictions, however. Accordingly, future experi-

Table 1. Computed Transition Frequencies (Shifted by $+36 \text{ cm}^{-1}$), Comparison with Experiment, and Qualitative Assignments for the Simulated Rovibrational Water–Iodide Spectrum at 20 K^a

peak [calc.]	peak [exp.]	calculated (cm ⁻¹)	experiment (cm ⁻¹)	initial state (calc.)	final state (calc.)	K_a
$lpha_{1a}$	-	3858	_	GS(-)	FOH + IP(+)	0 → 1
$lpha_1$	$oldsymbol{eta}_1$	3855	3855	GS(+)	FOH + IP(+)	II
$lpha_2$	eta_2	3829	3831	GS(-)	FOH + IP(-)	II
α_3	eta_3	3799	3815	GS(-)	FOH + IO(-)	II
$lpha_4$	eta_4	3768	3763	GS(+)	FOH(-)	$1 \rightarrow 2$
$lpha_5$	eta_{5}	3748	3744	GS(-)	FOH(+)	$1 \rightarrow 2$
$lpha_6$	eta_6	3735	3729	GS(+)	FOH(-)	$0 \rightarrow 1$
$lpha_7$	$oldsymbol{eta}_7$	3714	3714	GS(+)	FOH(+)	II
$lpha_8$	eta_8	3715	3705	GS(-)	FOH(+)	$0 \rightarrow 1$
$lpha_{8 ext{a}}$	_	3708	_	GS(+)	IHB + IP(-)	$1 \rightarrow 2$
α_9	eta_{9}	3701	3695	GS(+)	FOH(-)	$1 \rightarrow 0$
$lpha_{ m 10b}$	_	3682	_	GS(-)	FOH(+)	$1 \rightarrow 0$
$lpha_{10 ext{a}}$	_	3676	_	GS(+)	IHB + IP(-)	$0 \rightarrow 1$
$lpha_{10}$	eta_{10}	3668	3646	GS(+)	IHB + IP(+)	II
$lpha_{11}$	$oldsymbol{eta}_{11}$	3642	3636	GS(+)	IHB + IP(-)	$1 \rightarrow 0$
$lpha_{12}$	eta_{12}	3639	3633	GS(+)	2HOH + 2IP(+)	II
$lpha_{13}$	eta_{13}	3408	3438	GS(+)	IHB(+)	II
$lpha_{14}$	eta_{14}	3423	3426	GS(+)	2HOH + IP(+)	II
$lpha_{15}$	eta_{15}	3399	3406	GS(-)	IHB(-)	II
$lpha_{16}$	eta_{16}	3355	3396	GS(+)	2HOH + IO(+)	II
$lpha_{16a}$	_	3449	_	GS(+)	2HOH + 2IO(+)	II
$lpha_{17}$	$oldsymbol{eta}_{17}$	3258	3252	GS(+)	2HOH(+)	II
$lpha_{18}$	eta_{18}	3253	3248	GS(-)	2HOH(-)	II

^aThe assignments were made by projecting the calculated states onto the basis states listed in Tables S1.1 and S1.2. The \parallel notation represents a parallel transition with $\Delta K_a = 0$.

ments (possibly with higher-resolution lasers) that further disentangle the several, potentially overlapping transitions in this region are recommended.

Important discrepancies between the six-dimensional prediction and the observed spectra were also observed. For example, a transition in the calculated spectrum was observed between features α_9 and α_{11} , which is not evident in the experimental spectrum. This feature is assigned to transitions from GS(+) to levels with one quantum of excitation in the IHB and one quantum of excitation in the in-plane bend [IHB +IP(-) $K_a = 1 \leftarrow 0$]. In the region of the IHB quartet, the calculated linear spectrum additionally shows only three peaks—two originating from GS(+) and one from GS(-) that carry intensity, along with additional features that are close in energy. These and other smaller differences between the experimental and calculated spectrum likely reflect the sensitivity of the intensities of transitions to accidental resonances, which are, in turn, similarly sensitive to subtle features of the potential surface. In general, both the empirical analysis and the "ab initio" eigensolver approach were necessary in order to assign the rovibrational fine structure and line intensities as such. These comparisons establish important constraints that could perhaps be used to guide the continued feedback loop required to refine the potential energy surface.

CONCLUSIONS

The origins of the unexpected quartet in the $3400~\rm cm^{-1}$ region of the $I^-\cdot H_2O$ vibrational predissociation spectrum, which has eluded even qualitative assignment for nearly 25 years, were explored in the present study. New experimental approaches allowed for the resolution and assignment of the rotational structure in the FOH region of the spectrum. These

assignments enabled the determination of the ground-state tunneling splitting directly from the experimental spectrum to be roughly 20 cm⁻¹. This information, along with knowledge of the fundamental frequencies of all six normal modes, was used to provide tentative assignments of the four members of the quartet, including tunneling-split bands nominally associated with the bound OH stretch fundamentals as well as "extra" bands arising from coupling to nominally forbidden background states based on the v = 2 level of the HOH intramolecular bending mode. The intensity in each of the pairs of peaks is carried by the transitions from the two members of the ground-state tunneling doublet to states with one quantum of excitation in the IHB (the "bright states"), for which the tunneling splitting in the upper level is mostly quenched. The remaining two weaker features reflect transitions involving combination bands with two quanta in the HOH bend along with excitation of single quanta in the inplane bending or IO stretching modes. These findings were supported by two-color, IR-IR double-resonance experiments, which allowed for the separation of contributions to the spectrum from different symmetry classes of initial states. Finally, the spectra were compared to the results of high-level calculations of the rovibrational spectrum coupled with a recently available potential surface for $I^-\cdot H_2O$.

The many near-degeneracies in the spectrum of $I^- \cdot H_2 O$, particularly in the region of the quartet, place considerable spectroscopic demands on any potential energy surface—well beyond commonly accepted bounds for computed or measured thermochemical quantities. In addition, the prediction of experimental rovibrational spectra requires accurate treatment of the potential and dipole moment surfaces that govern the observed spectral patterns. The present attempt to generate the observed spectrum from first-

principles indicates that the existing halide—water potential perhaps needs refinement to achieve spectroscopic accuracy. Such refinements likely reflect the performance of the underlying quantum chemistry methods (section S1.1) that were used in the development of the many-body potential surface and not in the underlying model used to fit this potential. Nonetheless, the band pattern predicted by the full-dimensional eigensolver approach accurately recovered much of the character of the states that give rise to the observed multiplet fine structure in the experimental linear and state-specific double-resonance spectra. This combined effort involving application of advanced theoretical and experimental methods has thus unraveled the key, quantum mechanical motions at the heart of this long-standing spectroscopic puzzle in the microhydration of the iodide ion.

ASSOCIATED CONTENT

Solution Supporting Information

The Supporting Information is available free of charge at https://pubs.acs.org/doi/10.1021/acs.jpca.0c00853.

Computational details, including electronic structure method analysis, reference structures and vibrational coordinates, rovibrational spectroscopic simulation methods, vibrational state assignments, coordinates and normal-mode parameters, description of the vibrationally adiabatic model, and rotational structure simulations; experimental details; spectroscopic analysis, including rovibrational decomposition of the free—OH region, level structure, rotation constants, and calculated total spectrum (PDF)

AUTHOR INFORMATION

Corresponding Authors

Ryan P. Steele – Department of Chemistry and Henry Eyring Center for Theoretical Chemistry, University of Utah, Salt Lake City, Utah 84112, United States; orcid.org/0000-0002-3292-9805; Email: ryan.steele@utah.edu

Mark A. Johnson — Department of Chemistry, Yale University, New Haven, Connecticut 06520, United States; orcid.org/0000-0002-1492-6993; Email: mark.johnson@yale.edu

Anne B. McCoy — Department of Chemistry, University of Washington, Seattle, Washington 98195, United States; orcid.org/0000-0001-6851-6634; Email: abmccoy@uw.edu

Authors

Justin J. Talbot – Department of Chemistry and Henry Eyring Center for Theoretical Chemistry, University of Utah, Salt Lake City, Utah 84112, United States

Nan Yang — Department of Chemistry, Yale University, New Haven, Connecticut 06520, United States; orcid.org/0000-0003-1253-2154

Meng Huang — Department of Chemistry, University of Washington, Seattle, Washington 98195, United States; orcid.org/0000-0003-4318-5466

Chinh H. Duong — Department of Chemistry, Yale University, New Haven, Connecticut 06520, United States; ⊚ orcid.org/0000-0001-8026-1371

Complete contact information is available at: https://pubs.acs.org/10.1021/acs.jpca.0c00853

Author Contributions

"These authors contributed equally to this work.

Notes

The authors declare no competing financial interest.

ACKNOWLEDGMENTS

M.A.J. thanks the National Science Foundation under Grant CHE-1900119 for support of this work, which was carried out with the instrument developed under AFOSR DURIP Grant FA9550-17-1-0267. A.B.M. thanks the National Science Foundation for support under Grant CHE-1856124. Parts of this work were performed using the Ilahie cluster, which was purchased using funds from a MRI grant from the National Science Foundation (CHE-1624430). M.H. thanks The Ohio State University for support through a Presidential Fellowship. R.P.S. and J.J.T. acknowledge funding from the Department of Energy under Grant DE-SC0019405. The adiabatic vibrational analysis was also supported by National Science Foundation CAREER Grant CHE-1452596. The support and resources of the Center for High-Performance Computing at the University of Utah are gratefully acknowledged. This work also used the Extreme Science and Engineering Discovery Environment (XSEDE), which is supported by National Science Foundation Grant Number ACI-1548562.

REFERENCES

- (1) Johnson, M. S.; Kuwata, K. T.; Wong, C.-K.; Okumura, M. Vibrational Spectrum of I⁻(H₂O). *Chem. Phys. Lett.* **1996**, 260, 551–557.
- (2) Robertson, W. H.; Johnson, M. A. Molecular Aspects of Halide Ion Hydration: The Cluster Approach. *Annu. Rev. Phys. Chem.* **2003**, 54, 173–213.
- (3) Arismendi-Arrieta, D. J.; Riera, M.; Bajaj, P.; Prosmiti, R.; Paesani, F. I-TTM Model for Ab Initio-Based Ion—Water Interaction Potentials. 1. Halide—Water Potential Energy Functions. *J. Phys. Chem. B* **2016**, *120*, 1822—1832.
- (4) Ayala, R.; Martinez, J. M.; Pappalardo, R. R.; Sánchez Marcos, E. On the Halide Hydration Study: Development of First-Principles Halide Ion-Water Interaction Potential Based on a Polarizable Model. *J. Chem. Phys.* **2003**, *119*, 9538–9548.
- (5) Ayotte, P.; Weddle, G. H.; Kim, J.; Johnson, M. A. Vibrational Spectroscopy of the Ionic Hydrogen Bond: Fermi Resonances and Ion—Molecule Stretching Frequencies in the Binary X⁻⋅H₂O (X= Cl, Br, I) Complexes Via Argon Predissociation Spectroscopy. *J. Am. Chem. Soc.* **1998**, *120*, 12361–12362.
- (6) Bailey, C. G.; Kim, J.; Dessent, C. E.; Johnson, M. A. Vibrational Predissociation Spectra of $I^-(H_2O)$: Isotopic Labels and Weakly Bound Complexes with Ar and N_2 . Chem. Phys. Lett. **1997**, 269, 122–127.
- (7) Bajaj, P.; Wang, X.-G.; Carrington, T., Jr; Paesani, F. Vibrational Spectra of Halide-Water Dimers: Insights on Ion Hydration from Full-Dimensional Quantum Calculations on Many-Body Potential Energy Surfaces. *J. Chem. Phys.* **2018**, *148*, 102321.
- (8) Horvath, S.; McCoy, A. B.; Elliott, B. M.; Weddle, G. H.; Roscioli, J. R.; Johnson, M. A. Anharmonicities and Isotopic Effects in the Vibrational Spectra of X⁻· H₂O,· HDO, and· D₂O [X= Cl, Br, and I] Binary Complexes. *J. Phys. Chem. A* **2010**, *114*, 1556–1568.
- (9) Rheinecker, J. L.; Bowman, J. M. The Calculated Infrared Spectrum of Cl^-H_2O Using a Full Dimensional Ab Initio Potential Surface and Dipole Moment Surface. *J. Chem. Phys.* **2006**, 125, 133206.
- (10) Roscioli, J. R.; Diken, E. G.; Johnson, M. A.; Horvath, S.; McCoy, A. B. Prying Apart a Water Molecule with Anionic H-Bonding: A Comparative Spectroscopic Study of the X⁻·H₂O (X= OH, O, F, Cl, and Br) Binary Complexes in the 600−3800 cm⁻¹ Region. *J. Phys. Chem. A* **2006**, *110*, 4943−4952.

- (11) Sarka, J.; Lauvergnat, D.; Brites, V.; Császár, A. G.; Léonard, C. Rovibrational Energy Levels of the $F^-(H_2O)$ and $F^-(D_2O)$ Complexes. *Phys. Chem. Chem. Phys.* **2016**, 18, 17678–17690.
- (12) Thompson, W. H.; Hynes, J. T. Frequency Shifts in the Hydrogen-Bonded OH Stretch in Halide-Water Clusters. The Importance of Charge Transfer. J. Am. Chem. Soc. 2000, 122, 6278–6286.
- (13) Wolke, C. T.; Menges, F. S.; Tötsch, N.; Gorlova, O.; Fournier, J. A.; Weddle, G. H.; Johnson, M. A.; Heine, N.; Esser, T. K.; Knorke, H.; et al. Thermodynamics of Water Dimer Dissociation in the Primary Hydration Shell of the Iodide Ion with Temperature-Dependent Vibrational Predissociation Spectroscopy. *J. Phys. Chem. A* **2015**, *119*, 1859–1866.
- (14) Lee, H. M.; Kim, K. S. Structures and Spectra of Iodide—Water Clusters $I^-(H_2O)_{N=1-6}$: An Ab Initio Study. *J. Chem. Phys.* **2001**, *114*, 4461–4471.
- (15) Yang, N.; Duong, C. H.; Kelleher, P. J.; Johnson, M. A.; McCoy, A. B. Isolation of Site-Specific Anharmonicities of Individual Water Molecules in the $I^-\cdot(H_2O)_2$ Complex Using Tag-Free, Isotopomer Selective IR–IR Double Resonance. *Chem. Phys. Lett.* **2017**, 690, 159–171.
- (16) McCoy, A. B.; Guasco, T. L.; Leavitt, C. M.; Olesen, S. G.; Johnson, M. A. Vibrational Manifestations of Strong Non-Condon Effects in the $\rm H_3O^+\cdot X_3$ (X= Ar, N₂, CH₄, H₂O) Complexes: A Possible Explanation for the Intensity in the "Association Band" in the Vibrational Spectrum of Water. *Phys. Chem. Chem. Phys.* **2012**, *14*, 7205–7214.
- (17) Shao, Y.; Gan, Z.; Epifanovsky, E.; Gilbert, A. T.; Wormit, M.; Kussmann, J.; Lange, A. W.; Behn, A.; Deng, J.; Feng, X. Advances in Molecular Quantum Chemistry Contained in the Q-Chem 4 Program Package. *Mol. Phys.* **2015**, *113*, 184–215.
- (18) Stathopoulos, A.; McCombs, J. R. Primme: Preconditioned Iterative Multimethod Eigensolver—Methods and Software Description. ACM Transactions on Mathematical Software (TOMS) 2010, 37, 21.
- (19) Talbot, J. J.; Cheng, X.; Herr, J. D.; Steele, R. P. Vibrational Signatures of Electronic Properties in Oxidized Water: Unraveling the Anomalous Spectrum of the Water Dimer Cation. *J. Am. Chem. Soc.* **2016**, *138*, 11936–11945.
- (20) Wolk, A. B.; Leavitt, C. M.; Garand, E.; Johnson, M. A. Cryogenic Ion Chemistry and Spectroscopy. *Acc. Chem. Res.* **2014**, 47, 202–210.
- (21) Schlicht, F.; Entfellner, M.; Boesl, U. Anion ZEKE-Spectroscopy of the Weakly Bound Iodine Water Complex. *J. Phys. Chem. A* **2010**, *114*, 11125–11132.
- (22) Olkhov, R. V.; Nizkorodov, S. A.; Dopfer, O. Infrared Photodissociation Spectra of CH_3^+ -Ar_n Complexes (N = 1–8). *J. Chem. Phys.* **1998**, *108*, 10046–10060.
- (23) Bajaj, P.; Gotz, A. W.; Paesani, F. Toward Chemical Accuracy in the Description of Ion—Water Interactions through Many-Body Representations. I. Halide—Water Dimer Potential Energy Surfaces. *J. Chem. Theory Comput.* **2016**, *12*, 2698–2705.
- (24) Peterson, K. A.; Shepler, B. C.; Figgen, D.; Stoll, H. On the Spectroscopic and Thermochemical Properties of ClO, BrO, IO, and Their Anions. *J. Phys. Chem. A* **2006**, *110*, 13877–83.
- (25) Zare, R. N. Angular Momentum: Understanding Spatial Aspects in Chemistry and Physics; J. Wiley & Sons: 1988.
- (26) Western, C. M. PGOPHER: A Program for Simulating Rotational, Vibrational and Electronic Spectra. *J. Quant. Spectrosc. Radiat. Transfer* **2017**, *186*, 221–242.
- (27) Hamm, P.; Stock, G. Nonadiabatic Vibrational Dynamics in the HCO₂⁻·H₂O Complex. *J. Chem. Phys.* **2015**, *143*, 134308.
- (28) Pitzer, K. S.; Gwinn, W. D. Energy Levels and Thermodynamic Functions for Molecules with Internal Rotation I. Rigid Frame with Attached Tops. *J. Chem. Phys.* **1942**, *10*, 428–440.